frontiers in Energy Research

ORIGINAL RESEARCH
published: 02 September 2020
doi: 10.3389/fenrg.2020.570884

Dual Hydrogen- and Oxygen-Transport Membrane Reactor for Solar-Driven Syngas Production

*Maria Tou, Adrian Grylka, Arnaud Schuller, Brendan Bulfin, Aldo Steinfeld and Ronald Michalsky**

Department of Mechanical and Process Engineering, ETH Zürich, Zürich, Switzerland

A novel thermochemical dual-membrane reactor is considered with the goal of efficiently converting CO_2 to fuels using concentrated solar energy as the process heat source. In contrast to the temperature-swing redox cycle, in this isothermal system the thermolysis of H_2O at above 1,800 K is assisted by removal of O_2 across an oxygen-permeable membrane and of H_2 across a hydrogen-permeable membrane. The latter is consumed by a stream of CO_2 *via* the reverse water-gas shift reaction to re-form H_2O and continuously generate CO. The net reaction is the splitting of CO_2 to CO and $\frac{1}{2}O_2$. Because reactions at such high temperature are expected to be thermodynamically controlled, thermodynamic models are developed to calculate the equilibrium limits of the proposed dual-membrane configuration. For comparison, two reference configurations comprising either a single oxygen-permeable membrane or a single hydrogen-permeable membrane are analyzed. At 1,800 K, 1 bar total pressure, and (not applicable for the hydrogen-membrane reactor) 10 Pa O_2, the equilibrium mole fraction of fuel is 2% with a single oxygen membrane, 4% with a single hydrogen membrane, and 15% in the dual-membrane system. In all cases, total selectivity of CO_2 to CO and O_2 is obtained. Assuming thermodynamic equilibrium, the solar-to-fuel energy efficiency realistically attainable is 4% with a single oxygen membrane, 8% with a single hydrogen membrane, and 17% in the dual-membrane configuration at the aforementioned conditions. By increasing the pressure of the feed of steam to 100 bar, the dual-membrane model system could theoretically approach full mass conversion of CO_2 and reach up to 26% solar-to-fuel energy efficiency. However, developing appropriate and stable ceramic materials for such a system poses a significant challenge.

Keywords: solar fuels, thermolysis, membrane reactor, solar syngas, reverse water gas shift

OPEN ACCESS

Edited by:
Maurizio Troiano,
University of Naples Federico II, Italy

Reviewed by:
Qinghua He,
Auburn University, United States
Ligang Wang,
École Polytechnique Fédérale de Lausanne, Switzerland

****Correspondence:***
Ronald Michalsky
ronald.michalsky@gmail.com

Specialty section:
This article was submitted to Process and Energy Systems Engineering, a section of the journal Frontiers in Energy Research

Received: *09 June 2020*
Accepted: *17 August 2020*
Published: *02 September 2020*

Citation:
Tou M, Grylka A, Schuller A, Bulfin B, Steinfeld A and Michalsky R (2020) Dual Hydrogen- and Oxygen-Transport Membrane Reactor for Solar-Driven Syngas Production. Front. Energy Res. 8:570884. doi: 10.3389/fenrg.2020.570884

INTRODUCTION

Liquid hydrocarbon fuels are convenient energy carriers because of their high volumetric energy density, storability, and transportability with the existing global infrastructure. To that end, the formation of CO and H_2 (syngas) would be valuable as a feedstock for several established liquid fuel synthesis processes, such as Fischer-Tropsch or methanol synthesis. Research on various solar-driven approaches to convert CO_2 and H_2O to syngas has grown steadily as calls to reduce carbon emissions in the transportation and energy sector have intensified (Lewis, 2016). While solar

photovoltaics combined with electrolysis offers one commercialized option for producing H_2 from H_2O, an economically competitive solar technology to liquid fuels production from H_2O and CO_2 is still missing (Tuller, 2015).

The solar thermochemical approach to dissociate CO_2 and H_2O is promising because it utilizes the entire solar spectrum in the form of high-temperature process heat and, thus, enables thermodynamically favorable reactions and the potential of reaching high energy conversion efficiencies (Romero and Steinfeld, 2012). Specifically, a thermochemical membrane reactor suggests a path to isothermal and continuous splitting of CO_2 and H_2O, reactions described by

$$CO_2 \leftrightarrow CO + \frac{1}{2}O_2 \tag{1}$$

$$H_2O \leftrightarrow H_2 + \frac{1}{2}O_2 \tag{2}$$

In membrane-assisted thermolysis, one of the products is removed across a selective membrane to boost reaction conversion and prevent recombination. The idea to apply this concept to solar fuel production was pioneered by Fletcher and co-workers in the late 1970s (Fletcher and Moen, 1977; Noring et al., 1981). The first studies on solar thermal membrane reactors were theoretical in nature and focused on splitting H_2O (Fletcher and Moen, 1977; Noring et al., 1981; Kogan, 1997), and the vast majority of previous work has focused on oxygen-transport membranes (Franca et al., 2012; Muhich et al., 2013; Wang et al., 2015). This is because high-temperature oxygen-ion conducting materials are reasonably common, and their development has been propelled by applications in sensors, air separation (Sunarso et al., 2008; Geffroy et al., 2013), and solid-oxide fuel cells (Kharton et al., 2004; Garagounis et al., 2011). Recently, we have experimentally demonstrated the use of ceria-based oxygen-transport membranes in a solar cavity-receiver splitting CO_2 (Tou et al., 2017), and co-splitting CO_2 and H_2O simultaneously (Tou et al., 2019). However, the extent of H_2O and CO_2 thermolysis, even when enhanced by an oxygen-transport membrane, is impractically low at the required operating temperatures, typically in the range 1,500–2,000 K (Ermanoski et al., 2014; Li et al., 2019). For example, at a temperature of 2,000 K and a pressure of 1 bar, with oxygen extracted at a partial pressure of 3×10^{-5} bar, the thermodynamic limit for conversion of H_2O to H_2 is still only 5%.

The development of suitable hydrogen-permeable materials could improve the prospects of membrane reactor technology. In a 1981 study by Noring et al. (1981), a water-splitting reactor with two membranes, one each for oxygen and hydrogen removal was proposed. This combination significantly increases the driving force for thermolysis of H_2O and thus the theoretical fuel yield. Another benefit is the 100% purity of each product stream provided both membranes are perfectly selective. Nevertheless, the idea remained dormant for over three decades because the state-of-the-art could not supply stable materials at the temperatures required. Noring et al.'s concept applies uniquely to H_2O thermolysis because there has not been any research on CO-selective membranes that operate at and above 1,500 K to the knowledge of the authors. However, such a dual-membrane reactor (DMR) could still be useful for CO_2 splitting. The reactor system proposed by Noring et al. (1981) needs only a minor but nevertheless crucial modification: a feed of CO_2 introduced to the hydrogen chamber. Then, in addition to the thermolysis of H_2O in the steam chamber, CO_2 can react simultaneously with H_2 *via* the reverse water-gas shift (RWGS) reaction to produce CO:

$$H_2 + CO_2 \leftrightarrow CO + H_2O \tag{3}$$

Both reactions in Eqs 2 and 3 are enhanced by the transfer of H_2 across the membrane, and, in turn, drive further transport as they proceed. The net reaction is CO_2 splitting, as given in Eq. 1. To the authors' knowledge, such a membrane reactor concept is novel and could potentially become a breakthrough in this emerging field. Here we present a comparative thermodynamic analysis to understand how this DMR could work and to assess its performance potential. We also discuss the material challenges which researchers face to test this concept experimentally.

We select three representative configurations of a membrane reactor that could achieve the net reduction of CO_2: the DMR and two reference systems with a single membrane. For the sake of elucidating the key thermodynamics, the configurations are set up as three simple thought experiments as shown in **Figure 1**. In all cases, a closed volume is divided into chambers by semi-permeable boundaries—the membranes. Each chamber is filled with an initial amount of gases at set temperature T and pressure p. The system is then allowed to equilibrate at constant T and p. The walls are movable such that volumes can adjust freely as the number of molecules in each chamber changes (indicated by the spring symbol in **Figure 1**).

The first configuration is depicted in **Figure 1A**. Let's call the system the oxygen-membrane reactor (OMR). The simplest configuration of the three to be analyzed, the OMR contains two chambers, *0* and *I*, separated by an oxygen-permeable membrane. In chamber *0* a constant low value of p_{O_2} is maintained. An initial feed of CO_2, H_2O, or a combination thereof, is charged in chamber *I*. Given T and p, the feed dissociates to some extent to reach an equilibrium composition mixture of CO and/or H_2 and O_2, each exerting a corresponding partial pressure on the walls of chamber *I*. Assuming $p_{O_2,0}$ is set to a value less than $p_{O_2,I}$, a difference in chemical potential forms between the chambers, causing O_2 to diffuse across the membrane until the partial pressures balance on each side. However, this chemical potential equilibration *via* the removal of O_2 shifts the reaction equilibrium in chamber *I*, which must reach a new equilibrium based on the changed gas composition. According to Le Chatelier's principle, the reaction will proceed toward product formation. Any production of O_2 that results in $p_{O_2,I}$ exceeding $p_{O_2,0}$ also diffuses out of chamber *I*. Thus, the process continues until both chemical and mechanical equilibrium are reached in the OMR system. In this way, the oxygen-permeable membrane provides a way to drive the thermolysis reaction by controlling p_{O_2}. Note that the OMR is the closed-system analog of the oxygen-transport membrane reactor studied in other theoretical and experimental work (Evdou et al., 2008; Zhu et al., 2016; Tou et al., 2017; Tou et al., 2019).

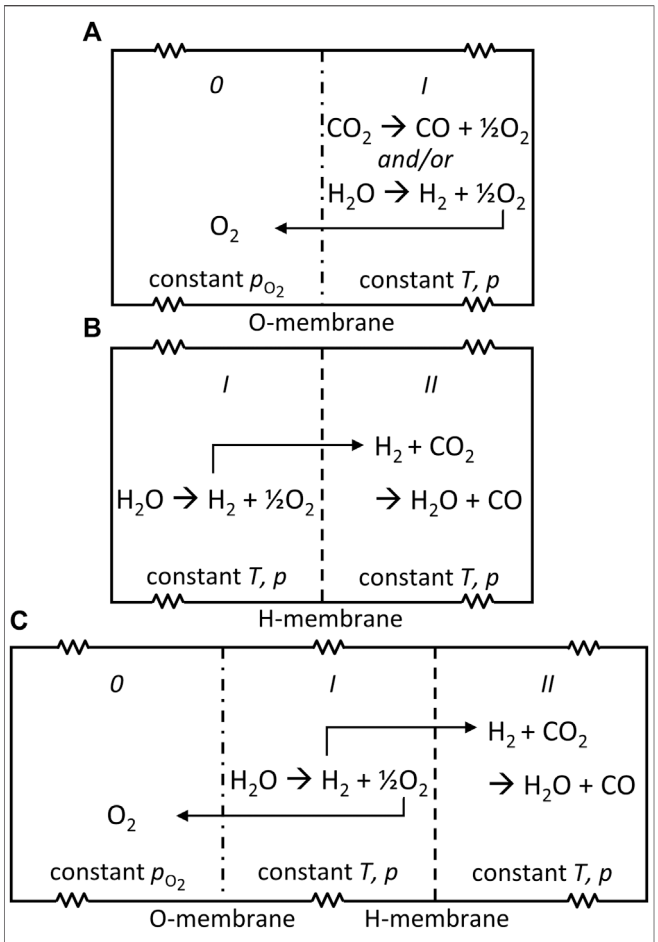

FIGURE 1 | Schematics of three configurations for the net thermochemical splitting of CO_2 to CO and O_2: **(A)** oxygen-membrane reactor, **(B)** hydrogen-membrane reactor, and **(C)** dual-membrane reactor. A spring symbol is used to indicate the free adjustment of volume in each chamber to maintain constant *p*.

The second configuration, shown in **Figure 1B**, follows the same principles as the first. Let's call it the hydrogen-membrane reactor (HMR). The HMR consists of two chambers, *I* and *II*, separated by a hydrogen-permeable membrane. Initially, chamber *I* contains H_2O and chamber *II* contains CO_2. *T* and *p* are controlled in each chamber. At these conditions, H_2O undergoes thermolysis like in the OMR. In this case, the equilibrium is shifted by the removal of H_2 as it diffuses to chamber *II*. Unlike the OMR, p_{H_2} is not set directly, but rather depends on another reaction equilibrium in chamber *II*: the RWGS reaction which consumes H_2 and CO_2 to produce CO and re-form H_2O. Thus, the overall reaction in the HMR is also the splitting of CO_2. The more H_2 is transferred from chamber *I* to *II*, the greater the extent of H_2O thermolysis (*via* removal of product) and of RWGS (*via* addition of reactant). The final state is reached once reactions and p_{H_2} have all equilibrated in both chambers. Thus, with the right choice of reactants, a hydrogen-permeable membrane can also drive the thermochemical conversion of CO_2 to CO.

The third configuration combines the OMR and HMR concepts to harness a dual driving force. The DMR shown in **Figure 1C** has three chambers, *0*, *I*, and *II*, demarcated by two membranes, one oxygen-selective and one hydrogen-selective. Each component behaves like its counterpart in the previous two configurations. However, now the thermolysis of H_2O in chamber *I* is enhanced by both the O_2 removal into chamber *0* and H_2 removal into chamber *II*, driven by differences in partial pressure of the respective species. The RWGS reaction consumes H_2 from chamber *I* to drive formation of CO in chamber *II*. At equilibrium, p_{O_2} must be equal in chambers *0* and *I*, and p_{H_2} must be equal in chambers *I* and *II*. Setting p_{O_2} in chamber *0* influences the extent of the RWGS reaction in chamber *II* by increasing the amount of H_2 available in chamber *I*. The DMR is the most complex of the three configurations, but may unlock higher reaction conversions and efficiencies in isothermal thermochemical processes. The next sections develop thermodynamic models and an efficiency analysis from these thought experiments to evaluate the DMR in comparison to the two single-membrane reference cases.

THERMODYNAMIC MODEL

The thermodynamic limits of the membrane reactor are governed by mass conservation and equilibrium relations, which, in turn, are dependent on the initial feed, temperature, total chamber pressures, and partial pressures of the components. We assume:

- closed system
- constant and uniform temperature and pressure in each chamber
- ideal gases
- well-mixed reactor chambers
- perfectly selective membranes
- thermodynamic equilibrium

The system as a whole is closed and at constant temperature and pressure, so that equilibrium will be the state with minimum Gibbs free energy, subject to mass balance constraints which are set by the initial conditions and the allowed chemical reactions. The Gibbs free energy is given by $G = \sum \mu_i n_i$, where μ_i and n_i are the chemical potential and number of moles of species *i*. Because the system is isothermal and the species are modeled as ideal gases, we can use

$$\mu_i(T) = \mu_i^\circ(T) + \mathrm{RT}\ln\left(\frac{p_i}{p^\circ}\right), \tag{4}$$

where μ_i° is the standard chemical potential at *T*, and the standard pressure p° is 1 bar. Therefore, we can conveniently switch to considering partial pressure differences across the membrane instead of chemical potentials, to check if species will favorably cross. By setting the Gibbs free energy of each expected reaction to zero ($\Delta G = 0$), together with mass balance constraints, this results in a system of equations defining the equilibrium state. The thermodynamic data needed (e.g., standard Gibbs free energies ΔG_i°) are available from the NIST JANAF thermochemical tables (Chase et al., 1998). The system can be solved analytically for the equilibrium composition, but to track molar amounts of all

species, including due to other potential side reactions, it becomes necessary to solve numerically.

Therefore, a second approach is implemented using thermodynamic software to account for all reactions possible starting from the initial composition. Cantera, a toolkit for chemical kinetics, thermodynamics, and transport problems, and its GRI-Mech 3.0 database (consisting of 53 species and 325 reactions detailing the natural gas combustion mechanism, including thermodynamic data for all species in the membrane reactor system) is called from Python and used for equilibrium composition calculations (Goodwin et al., 2009). To find the minimum Gibbs free energy we allow each chamber to go to chemical equilibrium separately, satisfying $\Delta G \leq 0$, and then check if there is a difference in chemical potential (partial pressure) of hydrogen across the hydrogen membrane and/or of oxygen across the oxygen membrane. If there is a difference, some of the membrane selective species Δn_i is transferred from higher to lower chemical potential so that $\Delta G = \Delta\mu_i \Delta n_i \leq 0$, where $\Delta\mu_i$ is the drop in chemical potential of the hydrogen or oxygen across the membrane. Each chamber is again allowed to go to equilibrium separately, and the process is repeated iteratively. In this way, we can converge on equilibrium in a finite number of steps, all of which satisfy $\Delta G \leq 0$, so that the entire process can proceed spontaneously.

Because the OMR and HMR serve as references for the DMR, and to avoid repetition, the OMR and HMR models are described in **Supplementary Figures S1,S2** and **Supplementary Tables S1,S2** and only the DMR model is detailed here. The model inputs are T, p, p_{O_2}, $n_{CO_2,i}$, and $n_{H_2O,i}$. The system of equations determining the equilibrium state without side reactions is summarized in **Table 1**. The Gibbs free energy relations for H_2O thermolysis and RWGS govern the composition of gases in chambers *I* and *II*, respectively. The hydrogen membrane links the thermodynamics of these chambers by enforcing a common p_{H_2}. The oxygen membrane adds an additional constraint by fixing p_{O_2}. Finally, the mole balances ensure that species are formed in stoichiometric amounts and account for mass transfer between chambers. The equations are formulated in terms of the fewest number of unknown variables by using the known stoichiometry of the reactions.

Figure 2 depicts the DMR model flow. Because there are two membranes, two sets of nested iterations are needed to determine the equilibrium state for the entire system. First, the reaction conditions and the initial feed are defined. Chambers *I* and *II* are equilibrated and the resulting $p_{O_2,I}$ is compared to $p_{O_2,0}$. Then, the value of $n_{O_2,I}$ is reset to get $p_{O_2,0}$ (simulating the removal of O_2) and the gas mixture is equilibrated again. Next, $p_{H_2,I}$ is compared to $p_{H_2,II}$. H_2 is transferred between chambers *I* and *II* to balance p_{H_2} and the new equilibrium state is calculated. This loop is repeated until $p_{H_2,I}$ converges to $p_{H_2,II}$, at which point p_{O_2} is checked again. Iterations stop once both loops simultaneously converge within their respective tolerances.

The model outputs are the equilibrium mole amounts of every species in each chamber, from which performance indicators can be calculated. The first is the mole fraction of fuel in the product mixture, which for the HMR and DMR is given by

$$x_{\text{fuel}} = \frac{n_{H_2,II} + n_{CO,II}}{N_{II} - n_{H_2O,II}} \tag{5}$$

For the HMR and DMR, x_{fuel} indicates the purity of the fuel produced, after condensation of the steam out of the syngas. For the OMR the fuel fraction is simply given by the mole fraction of CO or H_2, (e.g., $x_{\text{fuel}} = x_{CO}$). The second performance indicator is the fuel ratio in the product, H_2:CO, relevant only in cases where both H_2 and CO are produced. This quantity indicates which reaction is dominant at given conditions. Furthermore, its value is important for many downstream applications of syngas, and thus also indicates the amount of post-processing needed.

In the DMR, both H_2 and O_2 are removed from chamber *I* and conversion of H_2O could theoretically reach 100%. This implies that the number of moles in chamber *I* could approach zero. Because values close to zero cause numerical issues, a tolerance was set in the model to avoid infinite iteration. Another consequence of full conversion of H_2O is that it could limit the RWGS reaction in chamber *II*. That is, the equilibrium state

TABLE 1 | System of equations for the dual-membrane reactor.

Inputs	T, p, $p_{O_2,0}$, $n_{CO_2,i}$, $n_{H_2O,i}$
Equilibrium relations	
Chamber *I*	$K_W = \left(\frac{p_{H_2,I} \cdot p_{O_2,I}^{1/2}}{p_{H_2O,I}}\right) p^{\circ(-1/2)} = \exp\left(\frac{-\Delta G_W^{\circ}}{RT}\right)$
Chamber *II*	$K_{RWGS} = \left(\frac{p_{CO,II} \cdot p_{H_2O,II}}{p_{CO_2,II} \cdot p_{H_2,II}}\right) = \exp\left(\frac{-\Delta G_{RWGS}^{\circ}}{RT}\right)$
Membranes	$p_{O_2,0} = p_{O_2,I}$
	$p_{H_2,I} = p_{H_2,II}$
Mole balances	
Chamber *I*	$N_I = n_{H_2O,i} + n_{H_2,I} - (2n_{O_2,0} + n_{O_2,I})$
Chamber *II*	$N_{II} = n_{CO_2,i} + n_{H_2,II} + n_{H_2O,II}$
Overall	$0 = n_{H_2,I} + n_{H_2,II} + n_{CO,II} - 2(n_{O_2,0} + n_{O_2,I})$

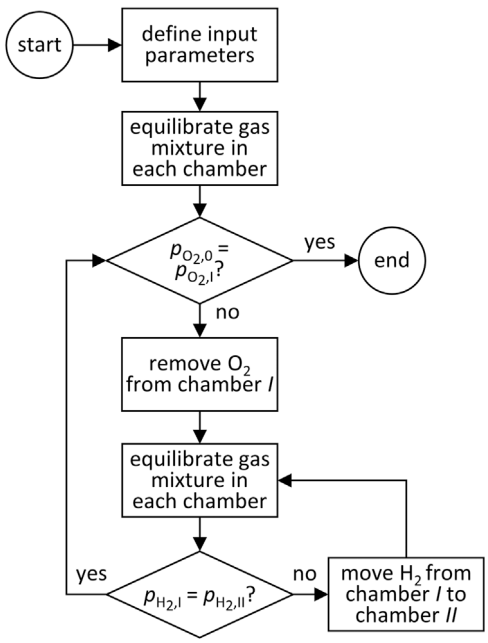

FIGURE 2 | A flowsheet illustrating the logic applied in the dual-membrane reactor equilibrium model.

has been reached for the given conditions and initial feed, but if there were additional H_2O relative to the CO_2 available, CO_2 would react further, and a different equilibrium composition would result. This means that there exists a minimum H_2O:CO_2 feed ratio to reach "unconstrained" equilibrium in the DMR. This dependence on H_2O:CO_2 is shown in **Supplementary Figure S6**.

THEORETICAL ENERGY EFFICIENCY ANALYSIS

Another critical performance indicator is the solar-to-fuel energy efficiency of the reactor, $\eta_{\text{solar-to-fuel}}$. Here, $\eta_{\text{solar-to-fuel}}$ is defined as the heating value of the fuel produced divided by the total heat input,

$$\eta_{\text{solar-to-fuel}} = \frac{n_{\text{fuel}}\text{HHV}_{\text{fuel}}}{Q_{\text{in}}}, \tag{6}$$

where the numerator is calculated using the appropriate higher heating value based on the amounts of CO and H_2 produced at equilibrium, and Q_{in} represents all heat and work heat-equivalents entering the solar reactor cavity. To define Q_{in}, a few assumptions must be made about the process, which is diagrammed with all possible process units in **Figure 3**. Thus, the solar-to-fuel energy efficiency is not a pure thermodynamic property. First, only solar radiation entering through the cavity's aperture is accounted for. That is, heliostat field losses are not included. The solar cavity-receiver is assumed to be a perfectly insulated blackbody absorber. Re-radiation losses from the cavity are included, but conductive and convective losses are neglected. It is assumed that the membrane reactor is operated in continuous parallel-flow mode and heat recovery from the exiting gases pre-heats the incoming streams. Low p_{O_2} is achieved by vacuum pumping. As an aside, low p_{O_2} can also be reached using an inert sweep gas. However, various studies have shown that sweeping is less efficient than pumping (Tan and Li, 2007; Bulfin et al., 2015). Furthermore, the most effective sweep gas is in counter-flow, and the calculation of the minimum flow rate of sweep gas to maintain a certain p_{O_2} is not trivial. As recently pointed out by Bulfin (2019) and Li et al. (2019), it has previously been incorrectly determined, resulting in overly optimistic sweep gas requirements. Both Bulfin (2019) and Li et al. (2019) describe thermodynamic analyses applicable to countercurrent reactors. In case the pressure of the CO_2-containing chamber is below atmospheric, a vacuum pump is again used. In case the pressure of a CO_2-containing chamber is above atmospheric, a compressor is needed. If the purity of the product is below a certain threshold, some unreacted CO_2 is removed in a separation process. Thus, Q_{in} is defined to include

$$Q_{\text{in}} = \frac{1}{\eta_{\text{abs}}}\left(Q_{\text{reaction}} + Q_{\text{sensible}} + Q_{\text{latent}}\right) + Q_{\text{pump,O}_2} + Q_{\text{pump,CO}_2} + Q_{\text{separation}} \tag{7}$$

The cavity absorption efficiency, η_{abs}, is only applied on the inputs added to the system in the form of concentrated solar heat: reaction enthalpy, Q_{reaction}; sensible heating of gases, Q_{sensible}; and

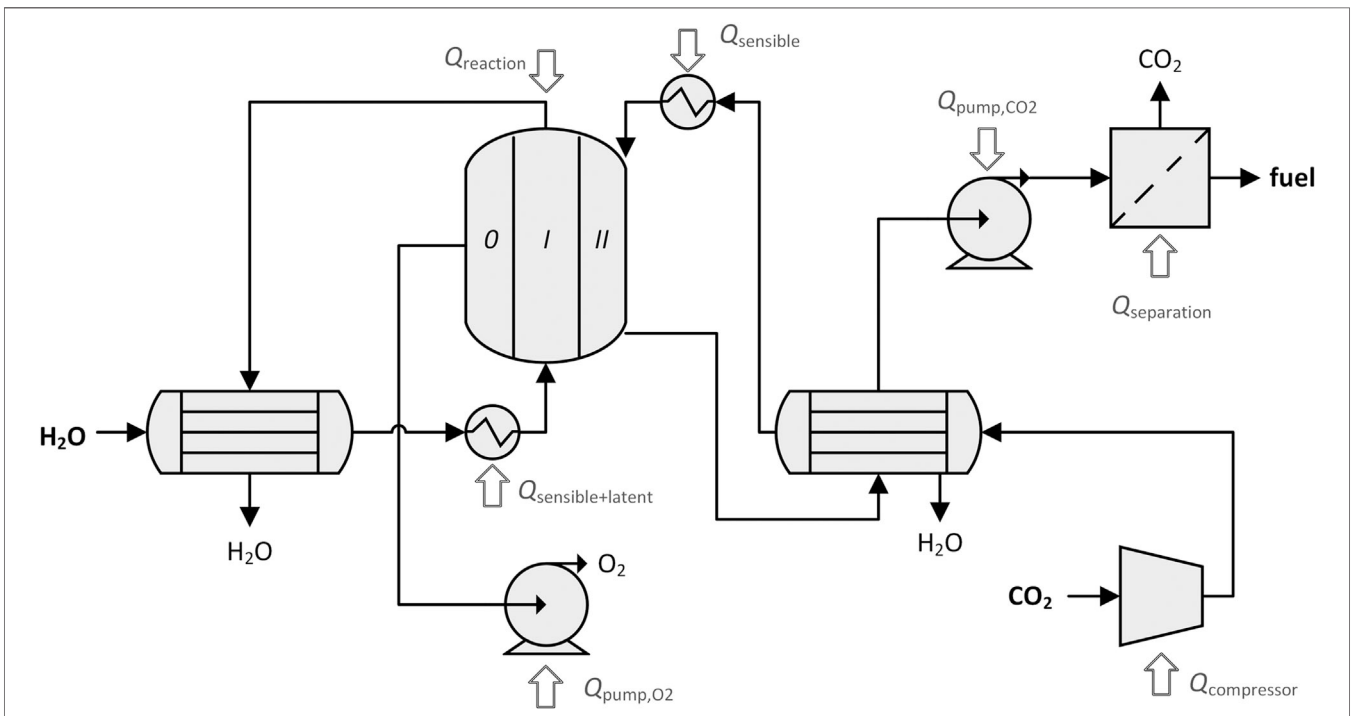

FIGURE 3 | Process diagram of the dual-membrane reactor including process units and heat inputs. Different subsets of these process units are applicable for different membrane configurations and operating conditions.

latent heat of vaporization of steam, Q_{latent}. The other inputs are work penalties converted to heat: heat equivalent to pump O_2 out of chamber *0*, Q_{pump,O_2}; heat equivalent to compress or pump a CO_2 chamber, Q_{pump,CO_2}; and heat equivalent to separate CO_2 from product to ensure sufficient fuel purity, $Q_{separation}$. Note that not all the components of total heat input are applicable in every membrane configuration.

As a blackbody absorber, re-radiation from the solar cavity is characterized by (Steinfeld and Palumbo, 2001):

$$\eta_{abs} = 1 - \frac{\sigma T^4}{IC}, \tag{8}$$

where σ is the Stefan-Boltzmann constant, I is the direct normal solar irradiation (DNI = 1 kW/m^2), and C is the solar concentration ratio. The reaction enthalpy is calculated for each reaction as

$$Q_{reaction} = \chi_{feed} n_{feed,i} \sum_i \nu_i h_{f,i}(T), \tag{9}$$

where χ_{feed} and n_{feed} are the conversion and the initial number of moles, respectively, ν_i is the stoichiometric coefficient of species i, and $h_{f,i}$ is the molar heat of formation of species i at T. The feed species refers to CO_2 or H_2O, depending on the reaction. The sum of $Q_{reaction}$ for each reaction in the system defines the total. Without heat recovery, heating is required to bring the feed species from ambient T_0 to reaction temperature T. The sensible portion is the total change in enthalpy less the latent heat of vaporization, if applicable:

$$Q_{sensible} = n_{feed,i}\left(h_{feed}(T) - h_{feed}(T_0) - \Delta h_{vap}\right). \tag{10}$$

For H_2O streams, the latent heat requirement is then:

$$Q_{latent} = n_{H_2O,i} \Delta h_{vap}. \tag{11}$$

With heat recovery, some fraction of the heat available in the outlet streams preheats the inlet to T_x, as determined by the heat recovery efficiency (Bader et al., 2013; Ermanoski et al., 2014; Venstrom et al., 2014; Bulfin et al., 2015):

$$\eta_{HEX} = \frac{n_{feed,i}\left(h_{feed}(T_x) - h_{feed}(T_0)\right)}{\sum_{i \text{ in outlet}} n_i \left(h_i(T) - h_i(T_0)\right)}, \tag{12}$$

where the denominator sums the change in enthalpy of each species in the outlet stream. Then, the sensible heating requirement is reduced to

$$Q_{sensible,HEX} = n_{feed,i}\left(h_{feed}(T) - h_{feed}(T_x)\right). \tag{13}$$

For an H_2O stream, we assume that the heat exchanger is used for latent heating first, and so this modification of $Q_{sensible}$ only applies if $h_{H_2O}(T_x) > \Delta h_{vap}$. Under that condition, the heat exchanger has the capacity to vaporize all of the H_2O, and $Q_{latent,HEX} = 0$. Otherwise, the latent heat requirement is

$$Q_{latent,HEX} = n_{H_2O,i}\left(\Delta h_{vap} - h_{H_2O}(T_x)\right). \tag{14}$$

In general, a heat input may not be negative, it may only be reduced to zero. Because the DMR has two gas streams, there are two possible arrangements for the two heat exchangers. In one, each outlet stream preheats its own inlet, as shown in **Figure 3**. In the other, streams are crossed in the heat exchangers so that one outlet stream preheats the opposite inlet and vice versa. Depending on the operating conditions, one of the arrangements may be favorable to maximize the amount of recovered heat.

The magnitude of the energy penalties in Q_{in} depend strongly on the assumptions made respecting the efficiency of their processes. Therefore, two cases are presented: the ideal case marking the thermodynamic limit and the more realistic case considering real processes and empirically observed efficiencies.

For vacuum pumping of a chamber to vacuum pressures, as done to control p_{O_2} in chamber *0* or to reduce p in another chamber, the minimum heat equivalent is based on isothermal expansion:

$$Q_{pump,ideal} = \frac{n_{pumped} R T_0}{\eta_{heat\text{-}to\text{-}work}} \ln\left(\frac{p_{atm}}{p_{pumped}}\right), \tag{15}$$

where n_{pumped} is the amount of gas pulled through the vacuum pump ($n_{O_2,0}$ for O_2 pumping), $\eta_{heat\text{-}to\text{-}work}$ is the heat-to-work conversion efficiency, p_{atm} is atmospheric pressure, and p_{pumped} is the desired pressure ($p_{O_2,0}$ for O_2 pumping). The empirical efficiency of vacuum pumping systems decreases strongly with decreasing vacuum pressure. Therefore, a realistic estimate of the pump work heat-equivalent is

$$Q_{pump,real} = \frac{Q_{pump,ideal}}{\eta_{pump}}, \tag{16}$$

where η_{pump} is determined by an envelope function fit to the empirical efficiency of vacuum pumps reported by Brendelberger et al. (2017). If CO_2 is fed at elevated pressure, the idealized heat equivalent for the pumping work is based on isentropic compression, because most compressors in industry are designed to run adiabatically (Campbell, 2014):

$$Q_{pump,CO_2,ideal} = \frac{n_{CO_2,i} C_p T_0}{\eta_{heat\text{-}to\text{-}work}} \left(\left(\frac{p_{pumped}}{p_{atm}}\right)^{R/C_p} - 1\right), \tag{17}$$

where C_p is the heat capacity of CO_2 and R is the ideal gas constant. $Q_{pump,CO_2,ideal}$ is scaled by a realistic compressor efficiency, $\eta_{compressor}$, to determine:

$$Q_{pump,CO_2,real} = \frac{Q_{pump,CO_2,ideal}}{\eta_{compressor}}. \tag{18}$$

Thermolysis reactions suffer from low molar conversions at insufficiently high T. Therefore, the gas mixture exiting the reactor may need purification. H_2O can be separated *via* condensation at low T and requires no additional work. CO_2 removal, on the other hand, requires an additional process. The minimum work to separate CO_2 from fuel in the product gas mixture is the difference in Gibbs free energy of mixing between the reactor outlet composition and the desired purity. Assuming any H_2O present in the product stream is previously removed, the gas mixture is treated as a binary mixture of fuel and CO_2:

$$Q_{\text{separation,ideal}} = \frac{RT_0}{\eta_{\text{heat-to-work}}}\left[\frac{n_{\text{fuel}}}{x'_{\text{fuel}}}\left(x'_{\text{fuel}}\ln x'_{\text{fuel}} + \left(1 - x'_{\text{fuel}}\right) \times \ln\left(1 - x'_{\text{fuel}}\right)\right) - N\left(x_{\text{fuel}}\ln x_{\text{fuel}} + \left(1 - x_{\text{fuel}}\right)\ln\left(1 - x_{\text{fuel}}\right)\right)\right], \quad (19)$$

where x_{fuel} and N are the mole fraction of fuel and total number of moles in the dehydrated product, respectively, and x'_{fuel} and $n_{\text{fuel}}/x'_{\text{fuel}}$ are the same quantities in the purified product. Determination of a realistic separation penalty is challenging, because there are few industrial examples of separating mixtures with comparable compositions. To approximate the magnitude of this quantity in this work, an amine-based adsorption process for the scrubbing of flue gases described by Rochelle et al. (2011) is taken as reference. Using the heat duty and work required for the scrubber, the separation heat equivalent is calculated to be approximated q_{scrubber} = 122 kJ/mol CO_2 removed. Thus,

$$Q_{\text{separation,real}} = n_{\text{CO}_2\text{,removed}} q_{\text{scrubber}}. \quad (20)$$

It is worth noting that the heating value of CO is 283 kJ/mol, which is the same order of magnitude as q_{scrubber}. Thus, $Q_{\text{separation,real}}$ can already be anticipated to have a large impact on $\eta_{\text{solar-to-fuel}}$.

RESULTS AND DISCUSSION

The thermodynamic equilibrium models and energy efficiency analysis form the basis of parametric studies to compare the DMR configuration to the single-membrane configurations and identify the operating conditions needed for best performance. The baseline values of the input parameters are summarized in **Table 2**, distinguishing between idealistic and realistic assumptions, where applicable. The chosen parameter sweep range is broad enough to demonstrate trends while simultaneously reflecting realistically attainable conditions. High T is needed to drive highly endothermic reactions, but the maximum T is limited by the solar concentration ratio (Steinfeld and Palumbo, 2001) and material stability considerations (Noring et al., 1981; Kalogirou, 2004). Therefore, here we focus on the range 1,500–2,000 K. For studies at constant T, 1800 K is used, considered the highest realistic operating T (Ermanoski et al., 2014; Marxer et al., 2017). Low p_{O_2} is favorable to drive O_2 removal, but the minimum is limited by the energy penalty of pumping at very low pressures (Brendelberger et al., 2017). Therefore, we consider the range 1–100 Pa O_2, and 10 Pa O_2 is used for studies at constant p_{O_2}. (From this point forward, p_{O_2} refers to the partial pressure of O_2 set in chamber *0*, i.e., $p_{O_2,0}$, unless otherwise specified.) However, we also look at some edge cases, especially when investigating the effect of p in different chambers. Atmospheric pressure is taken as a base case for all reaction chambers. Gas compression does not pose severe energy penalties to the process, but there is a maximum pressure difference that the membranes can mechanically withstand. While the membranes could be designed to be more robust, there is a foreseen tradeoff with diffusion rates. Because of the novelty of this type of membrane reactor, realistic limits on p are uncertain, and, therefore, a large range is explored.

Both thermodynamic modeling approaches yielded equivalent results, indicating that neglecting side reactions was justified. Details of the comparison of the two approaches are given in the **Supplementary Material** and **Supplementary Table S3**. **Figure 4** compares the OMR, HMR, and DMR on the basis of (**A**) x_{fuel} and (**B**) $\eta_{\text{solar-to-fuel}}$ under realistic assumptions, as functions of T. Note that if H_2O is fed to the OMR, the net reaction is water splitting, not CO_2 splitting. All chambers containing a chemical reaction are set to 1 bar total pressure. For the OMR and DMR, p_{O_2} is set to 10 Pa. This is not a free variable for the HMR. There, only H_2O:CO_2 can be controlled, and it is set to the value which maximizes $\eta_{\text{solar-to-fuel}}$ at each T considered. The same rationale is used for setting H_2O:CO_2 in the DMR.

In **Figure 4A**, x_{fuel} in the DMR is higher than in the other configurations over the entire range of T. This result could be expected because the OMR and HMR each depend on a driving force across a single membrane, whereas the DMR benefits from the combined driving force of both membranes. Furthermore, effectiveness of each single membrane can be evaluated by comparing the "HMR" and "OMR–CO_2" curves. At most T, driving the CO_2-splitting reaction with p_{H_2} leads to higher x_{fuel} than using p_{O_2}. This is partially because the amount of H_2 produced per mole of reaction exceeds O_2 by a factor of two, making it easier to create a large Δp across the membrane. In addition, the product stream in the HMR is a mixture of CO, H_2, CO_2, and H_2O, which is entropically favored over the mixture of CO and CO_2 in the OMR. However, reaction in the HMR is limited by the amount of H_2 able to cross the membrane at equilibrium, which depends on the thermolysis of H_2O. At high T, H_2O thermolysis is less favorable than CO_2 thermolysis, and

TABLE 2 | Baseline parameters used in thermodynamic efficiency analysis.

Parameter	Idealistic value //realistic value[a]	References
T	1,800 K	
p	1 bar	
p_{O_2}	10 Pa	
$n_{CO_2,i}$	1 mol	
$n_{H_2O,i}$	1 mol	
C	3,000 suns	Chase et al. (1998), Kharton et al. (2004), Zhu et al. (2016), Bulfin (2019)
η_{hex}	0.9	Chase et al. (1998)
$\eta_{\text{heat-to-work}}$	0.4	Kharton et al. (2004), Zhu et al. (2016)
η_{pump}	1 //$f(p_{\text{pumped}})$	Bader et al. (2013)
$\eta_{\text{compressor}}$	1 //0.85	Venstrom et al. (2014)
x'_{fuel}	0.5	
q_{scrubber}[b]	122 kJ/mol CO_2 removed	Brendelberger et al. (2017)

[a]*If only one value is given, the parameter is the same in the idealistic and realistic cases.*
[b]*Applicable in realistic case only.*

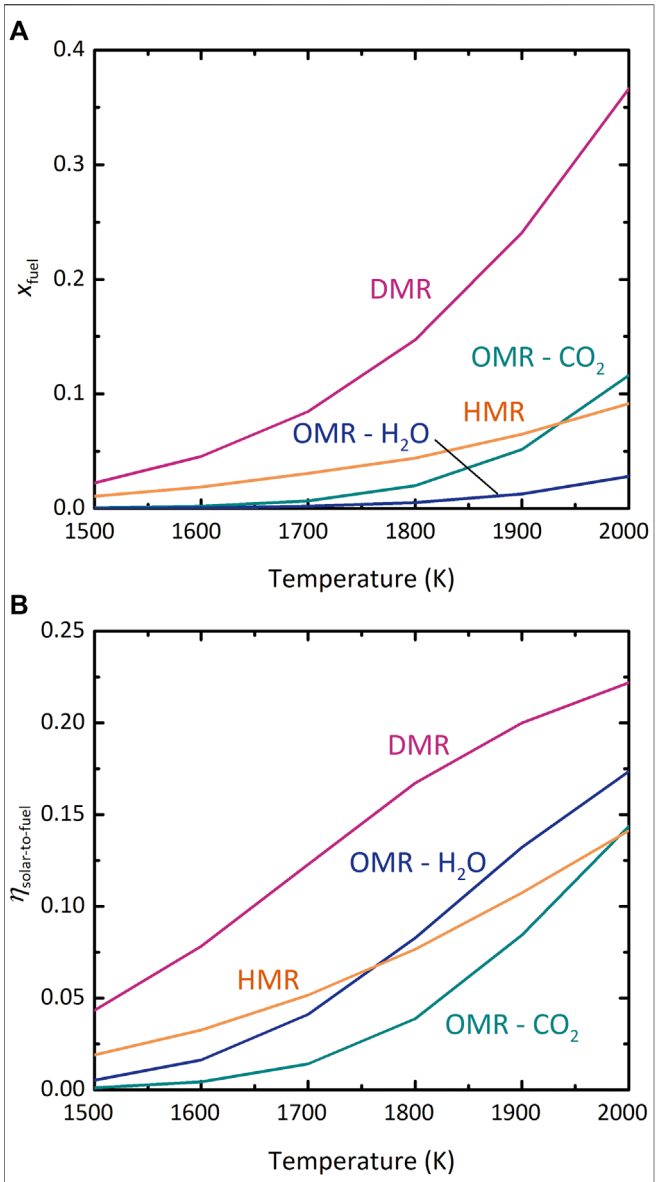

FIGURE 4 | Comparison of the oxygen-membrane reactor (OMR), hydrogen-membrane reactor (HMR), and dual-membrane reactor (DMR) configurations. **(A)** x_{fuel} vs. T, **(B)** $\eta_{solar\text{-}to\text{-}fuel}$ vs. T. p_I, p_{II} = 1 bar, where applicable. p_{O_2} = 10 Pa, where applicable. Where applicable, H_2O:CO_2 chosen to maximize $\eta_{solar\text{-}to\text{-}fuel}$ at each point.

the difference grows exponentially with T. Thus, x_{fuel} in the OMR overtakes that in the HMR above 1,900 K.

Figure 4B shows that the DMR also outperforms the OMR and HMR in terms of $\eta_{solar\text{-}to\text{-}fuel}$. Furthermore, in the OMR the realistic efficiency of H_2O splitting exceeds CO_2 splitting, a reversal from the results for x_{fuel}. Thermolysis of CO_2 is thermodynamically more favorable than of H_2O at these high temperatures, leading to higher x_{fuel}, but the greater energetic cost of separating unreacted CO_2 from the CO/CO_2 mixture relative to condensing steam out of the H_2/H_2O mixture counteracts this benefit, resulting in lower $\eta_{solar\text{-}to\text{-}fuel}$. This effect is also why a higher T is needed before the "OMR–CO_2" efficiency curve overtakes that of the HMR relative to **Figure 4A**. As expected, the DMR exhibits advantages over the single-membrane OMR and HMR designs. The rest of this work examines the behavior of the DMR more closely; results of the individual analyses of the OMR and HMR are available in the **Supplementary Material** and **Supplementary Figures S1–S5**.

Figure 5 shows the detailed contributions to Q_{in} at the maximum $\eta_{solar\text{-}to\text{-}fuel}$ for four scenarios. In case 1, p_I and p_{II} are equal at 1 bar. In case 2, p_I is 10 bar and p_{II} is 0.1 bar. The "X" applied to each case designates the alternative heat exchanger arrangement described in the efficiency analysis. Both case 1 and 1X include a large contribution for $Q_{separation}$, more than one-third of the total heat required, because x_{fuel} is not high enough at these conditions. Case 2 and 2X do not incur any separation energy penalty, because x_{fuel} is greater than the minimum specified in **Table 2**. Due to the higher conversion in case 2, $Q_{reaction}$ increases. The amount of O_2 removed is also higher, leading to a significantly higher proportion of heat input going to Q_{pump,O_2}. Case 2 includes a contribution of heat to vacuum pumping of chamber II, Q_{pump,CO_2}, which is unnecessary in case 1. In sum, when comparing these specific scenarios, investing in Q_{pump,CO_2} is worthwhile to avoid $Q_{separation}$ in the DMR. **Figure 5** further demonstrates that the choice of heat exchanger arrangement is not critical to the efficiency of the DMR. The sensible and latent heating of the gas streams only accounts for 10% or less of Q_{in}. Therefore, although arrangement "X" reduces the fraction of heat required for the gases (and eliminates it altogether in case 1X), the influence on overall efficiency is small.

Figure 6 shows the dependence in the DMR of x_{fuel} and $\eta_{solar\text{-}to\text{-}fuel}$ on T at various p_{O_2}.Here both p_I and p_{II} are constant at 1 bar. x_{fuel} increases monotonically with increasing T and decreasing p_{O_2}, as expected from the equilibrium relationship of the reaction. At these conditions, $\eta_{solar\text{-}to\text{-}fuel}$ also

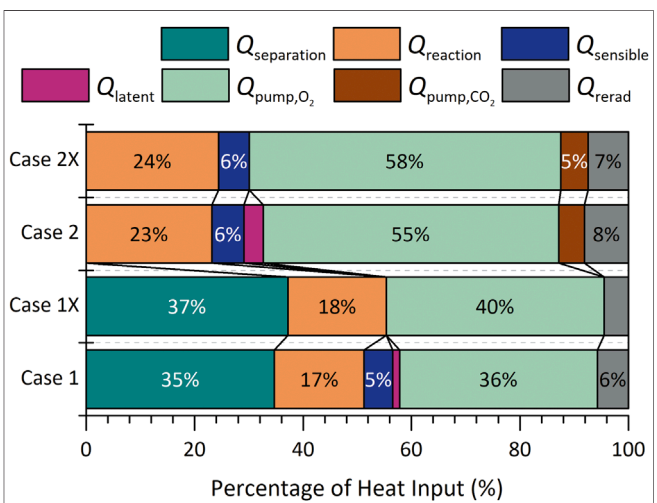

FIGURE 5 | Distribution of the components of Q_{in} for the dual-membrane reactor. Case 1: $p_I = p_{II}$ = 1 bar. Case 2: p_I = 10 bar, p_{II} = 0.1 bar. The suffix "X" denotes the cross-stream arrangement of heat exchangers, whereas in the standard arrangement the inlet and outlet of the same stream exchange heat. T = 1,800 K and p_{O_2} = 10 Pa.

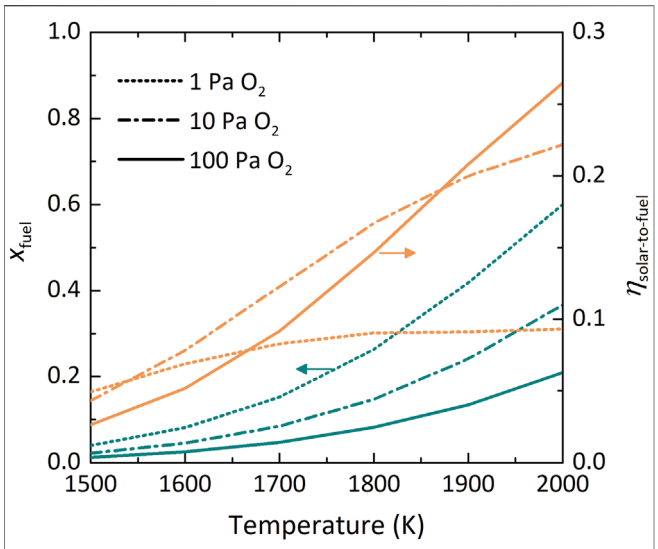

FIGURE 6 | Dual-membrane reactor performance indicators x_{fuel} (teal) and $\eta_{solar\text{-}to\text{-}fuel}$ (orange) as a function of T at various p_{O_2}. $p_I = p_{II} = 1$ bar.

increases with T, but with decreasing slope because at some point a maximum will be reached due to re-radiation from the cavity. The effect of p_{O_2} on $\eta_{solar\text{-}to\text{-}fuel}$ is not necessarily monotonic and changes with T. At the lowest T considered in **Figure 6**, 1,500 K, $\eta_{solar\text{-}to\text{-}fuel}$ increases as p_{O_2} decreases, but at the highest T of 2,000 K, the trend is reversed and $\eta_{solar\text{-}to\text{-}fuel}$ decreases as p_{O_2} decreases. Thus, the p_{O_2} that maximizes $\eta_{solar\text{-}to\text{-}fuel}$ increases with T. While decreasing p_{O_2} increases the fuel output of the reactor, it also demands pump work input to the reactor. At low T, the improvement in fuel production justifies the additional work to reduce p_{O_2}. However, as the amount of O_2 to be removed increases at higher T, there is a point where maintaining p_{O_2} requires more energy than is gained from the heating value of the fuel. For example, at a reference T of 1,800 K and a p_{O_2} of 1 Pa, x_{fuel} exceeds 20%, but $\eta_{solar\text{-}to\text{-}fuel}$ is less than 10%. If at the same T the p_{O_2} were increased to 10 Pa, x_{fuel} would drop to 15%, but $\eta_{solar\text{-}to\text{-}fuel}$ would almost double.

Figure 7 shows the effect of the ratio of pressures in chambers I and II on the three performance indicators: (**A**) x_{fuel}, (**B**) H_2:CO molar ratio, and (**C**) $\eta_{solar\text{-}to\text{-}fuel}$. T and p_{O_2} are constant at 1,800 K and 10 Pa, respectively. Results are grouped by the value of p_I. The plots show that, with the exception of $\eta_{solar\text{-}to\text{-}fuel}$ at high p_I:p_{II} in **Figure 7C**, the absolute values of p_I and p_{II} do not matter, but only the ratio between them, because the data collapse onto a single curve. As p_I:p_{II} increases, x_{fuel} and H_2:CO shown in **Figures 7A,B**, respectively, also increase until CO_2 is fully consumed and then they level off. At these conditions the threshold is at a 200:1 p_I-to-p_{II} ratio. Manipulation of p_I:p_{II} seems to be effective to drive the reaction to completion, as x_{fuel} reaches a maximum value of 1 in **Figure 7A**. As seen in **Figure 7B**, control over p_I:p_{II} also allows a broad range of H_2:CO ratios from 0.04 to 26 to become accessible, including industrially relevant ratios around 2 (Schulz, 1999; Leckel, 2009). In **Figure 7C**, $\eta_{solar\text{-}to\text{-}fuel}$ varies over a relatively smaller range than the other performance indicators, between 17 and 26%. $\eta_{solar\text{-}to\text{-}fuel}$ reaches a maximum at the same threshold ratio as observed

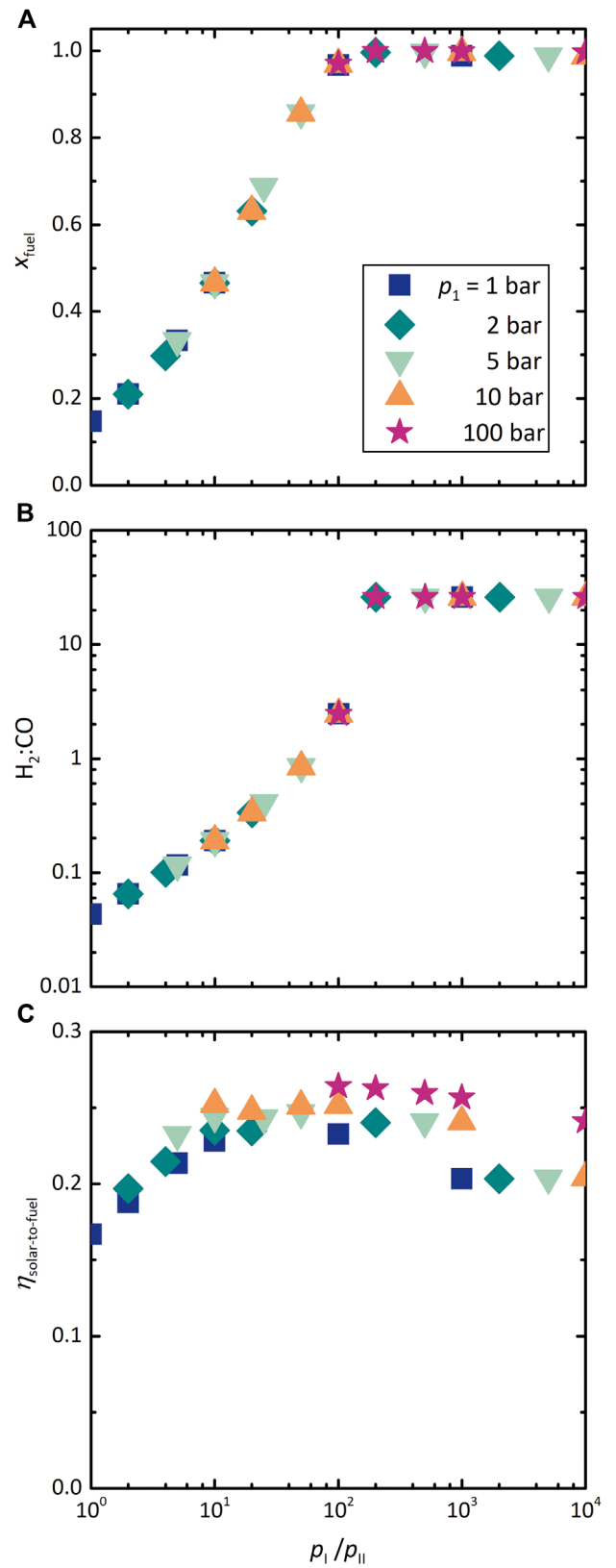

FIGURE 7 | Effect of the dual-membrane reactor chamber pressure ratio, p_I:p_{II}, on **(A)** x_{fuel}, **(B)** H_2:CO molar ratio, and **(C)** $\eta_{solar\text{-}to\text{-}fuel}$ at various values of p_I. T = 1,800 K and p_{O_2} = 10 Pa.

for x_{fuel} and H_2:CO. At lower values of p_I:p_{II}, the different values of p_I have similar efficiencies. However, it is already apparent that lower p_I leads to lower $\eta_{solar\text{-}to\text{-}fuel}$. At higher values of p_I:p_{II}, this trend becomes very clear, as the $\eta_{solar\text{-}to\text{-}fuel}$ at lower p_I falls more steeply. This effect is a consequence of increasing pumping cost in chamber *II* as p_{II} decreases, which is the case when p_I decreases at constant p_I:p_{II}. Keeping p_I greater than p_{II} is always thermodynamically beneficial, therefore there is no reason to consider doing work to evacuate H_2O in chamber *I* below atmospheric pressure, or to compress CO_2 in chamber *II* above atmospheric pressure. Moreover, changing p_I above atmospheric pressure does not affect heat requirements, because the feed to chamber *I* is produced by vaporizing H_2O. Therefore, assuming it is feasible to withstand large Δp across the membrane, efficiency is maximized by increasing p_I and keeping p_{II} atmospheric.

MATERIALS OUTLOOK

Although the values of process parameters used here were chosen to be as realistic as possible, there are nevertheless many idealistic assumptions in this theoretical analysis. The most optimistic assumption is that materials for such high-temperature, selective membranes exist. To test the actual capabilities and limitations of the membrane reactor, functional membranes are first necessary. Kinetics, material stability, and membrane selectivity will affect the performance of a physical system. Oxygen-conducting membranes based on nonstoichiometric ceria have been characterized and demonstrated for solar-driven thermolysis of CO_2 and H_2O (Tou et al., 2017; Tou et al., 2019). The analog for hydrogen at these operating conditions has not emerged, but some insight may be gained from neighboring fields.

Hydrogen-conducting membrane materials have been studied in the context of sensors, hydrogen fuel cells, electrolyzers, and (de)hydrogenation reactions (Liu et al., 2006). Dense metallic membranes show high conductivity and selectivity of H^+, but are limited to operation below 1,000 K. Furthermore, they are often Pd-based, which is expensive and impractical at the industrial scale (Tao et al., 2015). Considering the small size of H_2, selective transport based on molecular sieving through micropores has also been suggested (Fletcher and Moen, 1977; Kogan, 1997; Tao et al., 2015). Here, controlling pore size and stability is a challenge, and perfect selectivity impossible (Kogan, 1998). Dense ceramics have also been shown to conduct H^+, and are the only class of hydrogen-conductors stable at 1,800 K. Despite their own set of challenges, these mixed protonic-electronic conducting (MPEC) materials appear the most promising for hydrogen-conducting membranes.

Research has focused on perovskites, many of which are oxygen ion conductors. The compositions of perovskites that conduct hydrogen are limited, most often with Ba or Sr on the A site and Ce or Zr on the B site of the characteristic ABO_3 structure (Iwahara et al., 1982; Fabbri et al., 2010; Dong et al., 2011). Several studies identified $BaCe_{0.2}Zr_{0.7}Y_{0.1}O_3$ (BCZY27) to be a promising composition (Dippon et al., 2016). Ba-based perovskites have the highest proton conductivities, but their electron conductivity tends to limit the overall transfer of hydrogen (Fabbri et al., 2010). For better electron conductivity, the B site is often doped with a trivalent dopant such as Y (Dong et al., 2011). Due to tradeoffs in protonic and electronic mobility, the optimal temperature range for proton conduction in MPECs is about

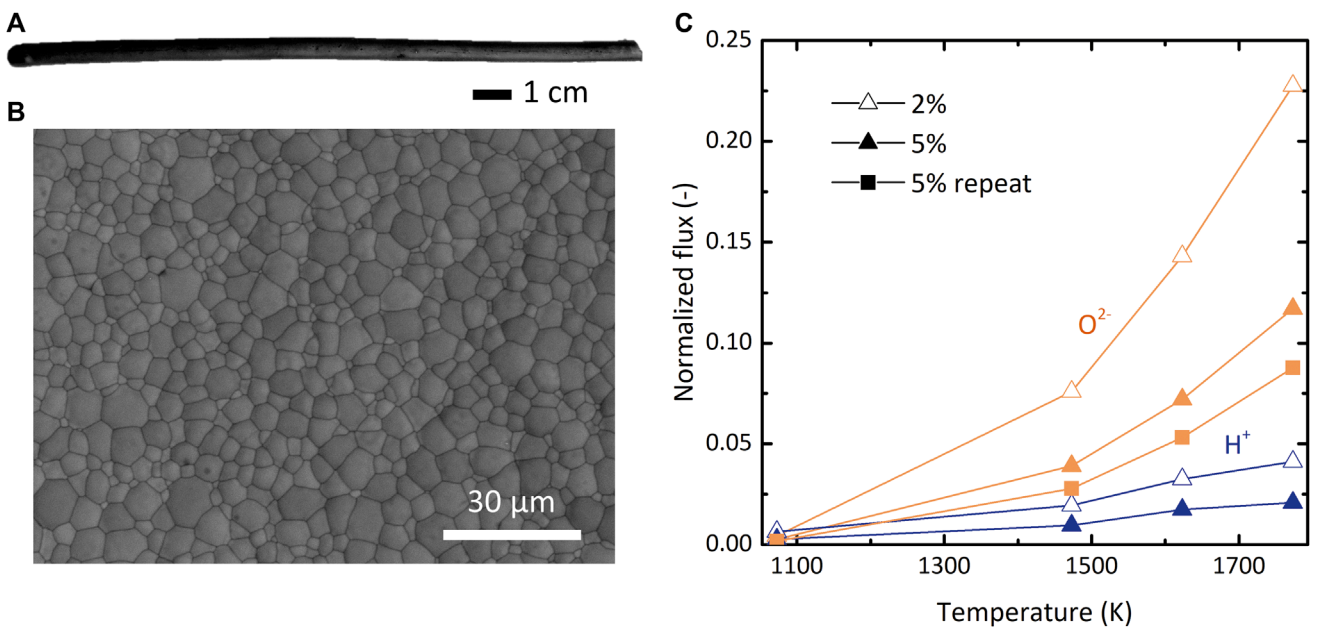

FIGURE 8 | (A) Photograph of a representative BCZY27 membrane, which were tubular and closed on one end. **(B)** Scanning electron microscopic image of the inner surface of a BCZY27 membrane. **(C)** Normalized ionic flux of H^+ (blue) and O^{2-} (orange) at the respective H_2 or O_2 feed gas concentrations of 2% (hollow) and 5% (solid) through a BCZY27 membrane as a function of *T*. A repetition of 5% O_2 feed with a different membrane is shown with square symbols.

673–873 K (Bonanos and Poulsen, 1999; Fabbri et al., 2010). Even then, the flux of hydrogen through these materials is considered impractically low and requires membrane thicknesses on the μm-scale (Phair and Badwal, 2006; Dong et al., 2011). Furthermore, studies have found that Ba-based perovskites also conduct O^{2-} at high temperatures, which is detrimental for our desired application in H_2O thermolysis (Fabbri et al., 2010).

To check the behavior of an MPEC material at temperature conditions needed for membrane-assisted thermolysis, we prepared tubular BCZY27 membranes and tested them in a set of simple permeation experiments (experimental details in the **Supplementary Material**). **Figures 8A,B** show a photograph and a scanning electron microscopic image of representative membranes. As shown in **Figure 8C**, BCZY27 indeed conducts O^{2-}, and in fact the measured flux of O^{2-} is higher than H^+ in the relevant range tested 1,073–1,773 K. Although the membrane thickness (~800 μm) likely limited hydrogen diffusion, more importantly, these experiments revealed a critical lack of selectivity. In sum, the practicality of the DMR depends on the development of hydrogen-selective, high-temperature membranes, and more materials science research to this end is still necessary.

SUMMARY AND CONCLUSIONS

We examined the concept of a thermochemical membrane reactor to split CO_2 and produce solar fuels from a thermodynamic perspective for three configurations: a single oxygen-permeable membrane (OMR), a single hydrogen-permeable membrane (HMR), and an oxygen-permeable and hydrogen-permeable dual-membrane (DMR) configuration. The theoretical solar-to-fuel energy efficiency calculations for all configurations assumed thermodynamic equilibrium and made realistic process assumptions to highlight process limitations. Low product purity in the OMR at all realistic operating conditions leads to low $\eta_{\text{solar-to-fuel}}$ of CO_2 thermolysis. The performance of the HMR depends on the choice of feed ratio, H_2O:CO_2, and values of x_{fuel} and $\eta_{\text{solar-to-fuel}}$ are expected to be below 15%. As expected, the DMR outperformed the OMR and HMR. The thermodynamic model identified non-unique operating conditions where χ_{CO_2} and x_{fuel} in the DMR could exceed 90%. One example is at 1,800 K, 10 Pa O_2 in chamber *0*, 100 bar total in chamber *I*, and 1 bar total in chamber *II*, where $\eta_{\text{solar-to-fuel}}$ reaches 26%. The same efficiency was predicted at 2,000 K, 100 Pa O_2 in chamber *0*, and 1 bar total in chambers *I* and *II*, where in this case x_{fuel} was 21%. The determination of the "best" operating conditions depends on physical feasibility. Reactor temperatures of 2,000 K like in the latter case are not currently possible. It also remains an open question whether membranes can be built that withstand extreme pressure differences like the one in the former case. More pressingly, suitable materials need to be developed, particularly for the hydrogen-permeable membrane.

DATA AVAILABILITY STATEMENT

All datasets presented in this study are included in the article/supplementary material.

AUTHOR CONTRIBUTIONS

MT wrote the manuscript, and developed the model together with her colleagues. She also performed the experimental work. AG did his master's thesis with MT, working on the thermodynamic models discussed in the manuscript. ArS, performed experimental work on membranes and assisted with the modeling work. BB formulated the approach to the modeling together with MT, and assistant in writing the manuscript. AlS co-supervised the work and assisted in writing the manuscript. RM co-supervised the work and assisted in writing the manuscript.

FUNDING

This work was funded by the Swiss National Science Foundation (Ambizione Energy Grant No. 166883).

ACKNOWLEDGMENTS

We thank Noah Oswald and Severin Kull for helping develop the experimental procedure.

SUPPLEMENTARY MATERIAL

The Supplementary Material for this article can be found online at: https://www.frontiersin.org/articles/10.3389/fenrg.2020.570884/full#supplementary-material

REFERENCES

Bader, R., Venstrom, L. J., Davidson, J. H., and Lipiński, W. (2013). Thermodynamic analysis of isothermal redox cycling of ceria for solar fuel production. *Energy Fuels* 27 (9), 5533–5544. doi:10.1021/ef400132d.

Bonanos, N., and Poulsen, F. W. (1999). Considerations of defect equilibria in high temperature proton-conducting cerates. *J. Mater. Chem.* 9, 431–434. doi:10.1039/a805150j.

Brendelberger, S., von Storch, H., Bulfin, B., and Sattler, C. (2017). Vacuum pumping options for application in solar thermochemical redox cycles – assessment of mechanical-, jet- and thermochemical pumping systems. *Solar Energy* 141, 91–102. doi:10.1016/j.solener.2016.11.023.

Bulfin, B. (2019). Thermodynamic limits of countercurrent reactor systems, with examples in membrane reactors and the ceria redox cycle. *Phys. Chem. Chem. Phys.* 21, 2186–2195. doi:10.1039/c8cp07077f.

Bulfin, B., Call, F., Lange, M., Lübben, O., Sattler, C., Pitz-Paal, R., et al. (2015). Thermodynamics of CeO_2 thermochemical fuel production. *Energy Fuels* 29 (2), 1001–1009. doi:10.1021/ef5019912.

Campbell, J. M. (2014). *Gas conditioning and processing: the equipment modules*. 9th Edn. Editors R. Hubbard and K. Snow-McGregor (Norman, OK: Campbell Petroleum Series), Vol. 2.

Chase, M. W., Davies, C. A., Downey, J. R., Frurip, D. J., McDonald, R. A., and Syverud, A. N. (1998). *NIST-JANAF thermochemical tables: NIST standard reference database 13. Standard reference data program*. National Institute of Standards and Technology.

Dippon, M., Babiniec, S. M., Ding, H., Ricote, S., and Sullivan, N. P. (2016). Exploring electronic conduction through $BaCe_xZr_{0.9-x}Y_{0.1}O_{3-d}$ proton-conducting ceramics. *Solid State Ion.* 286, 117–121. doi:10.1016/j.ssi.2016.01.029.

Dong, X., Jin, W., Xu, N., and Li, K. (2011). Dense ceramic catalytic membranes and membrane reactors for energy and environmental applications. *Chem. Commun.* 47 (39), 10886–10902. doi:10.1039/c1cc13001c.

Ermanoski, I., Miller, J. E., and Allendorf, M. D. (2014). Efficiency maximization in solar-thermochemical fuel production: challenging the concept of isothermal water splitting. *Phys. Chem. Chem. Phys.* 16 (18), 8418–8427. doi:10.1039/c4cp00978a.

Evdou, A., Nalbandian, L., and Zaspalis, V. (2008). Perovskite membrane reactor for continuous and isothermal redox hydrogen production from the dissociation of water. *J. Membr. Sci.* 325 (2), 704–711. doi:10.1016/j.memsci.2008.08.042.

Fabbri, E., Pergolesi, D., and Traversa, E. (2010). Materials challenges toward proton-conducting oxide fuel cells: a critical review. *Chem. Soc. Rev.* 39 (11), 4355–4369. doi:10.1039/b902343g.

Fletcher, E. A., and Moen, R. L. (1977). Hydrogen and oxygen from water. *Science* 197 (4308), 1050–1056. doi:10.1126/science.197.4308.1050

Franca, R. V., Thursfield, A., and Metcalfe, I. S. (2012). $La_{0.6}Sr_{0.4}Co_{0.2}Fe_{0.8}O_{3-\delta}$ microtubular membranes for hydrogen production from water splitting. *J. Membr. Sci.* 389, 173–181. doi:10.1016/j.memsci.2011.10.027.

Garagounis, I., Kyriakou, V., Anagnostou, C., Bourganis, V., Papachristou, I., and Stoukides, M. (2011). Solid electrolytes: applications in heterogeneous catalysis and chemical cogeneration. *Ind. Eng. Chem. Res.* 50 (2), 431–472. doi:10.1021/ie1001058.

Geffroy, P.-M., Fouletier, J., Richet, N., and Chartier, T. (2013). Rational selection of MIEC materials in energy production processes. *Chem. Eng. Sci.* 87, 408–433. doi:10.1016/j.ces.2012.10.027.

Goodwin, D. G., Moffat, H. K., and Speth, R. L. (2009). Cantera: an object-oriented software toolkit for chemical kinetics, thermodynamics, and transport processes. Pasadena, CA: Caltech.

Iwahara, H., Uchida, H., and Maeda, N. (1982). High temperature fuel and steam electrolysis cells using proton conductive solid electrolytes. *J. Power Sources* 7, 293–301. doi:10.1016/0378-7753(82)80018-9.

Kalogirou, S. A. (2004). Solar thermal collectors and applications. *Prog. Energy Combust. Sci.* 30 (3), 231–295. doi:10.1016/j.pecs.2004.02.001.

Kharton, V., Marques, F., and Atkinson, A. (2004). Transport properties of solid oxide electrolyte ceramics: a brief review. *Solid State Ion.* 174 (1–4), 135–149. doi:10.1016/j.ssi.2004.06.015.

Kogan, A. (1997). Direct solar thermal splitting of water and on site separation of the products – I. Theoretical evaluation of hydrogen yield. *Int. J. Hydrogen Energy* 22 (5), 481–486. doi:10.1016/s0360-3199(96)00125-5.

Kogan, A. (1998). Direct solar thermal splitting of water and on-site separation of the products – II. Experimental feasibility study. *Int. J. Hydrogen Energy* 23 (2), 89–98. doi:10.1016/s0360-3199(97)00038-4.

Leckel, D. (2009). Diesel production from Fischer-Tropsch: the past, the present, and new concepts. *Energy Fuels* 23, 2342–2358. doi:10.1021/ef900064c.

Lewis, N. S. (2016). Research opportunities to advance solar energy utilization. *Science* 351 (6271), aad1920. doi:10.1126/science.aad1920.

Li, S., Kreider, P. B., Wheeler, V. M., and Lipiński, W. (2019). Thermodynamic analyses of fuel production via solar-driven ceria-based nonstoichiometric redox cycling: a case study of the isothermal membrane reactor system. *J. Sol. Energy Eng.* 141 (2), 021012. doi:10.1115/1.4042228.

Liu, Y., Tan, X., and Li, K. (2006). Mixed conducting ceramics for catalytic membrane processing. *Catal. Rev.* 48 (2), 145–198. doi:10.1080/01614940600631348.

Marxer, D., Furler, P., Takacs, M., and Steinfeld, A. (2017). Solar thermochemical splitting of CO_2 into separate streams of CO and O_2 with high selectivity, stability, conversion, and efficiency. *Energy Environ. Sci.* 10 (5), 1142–1149. doi:10.1039/c6ee03776c.

Muhich, C. L., Evanko, B. W., Weston, K. C., Lichty, P., Liang, X., Martinek, J., et al. (2013). Efficient generation of H_2 by splitting water with an isothermal redox cycle. *Science* 341, 540–542. doi:10.1126/science.1239454.

Noring, J. E., Diver, R. B., and Fletcher, E. A. (1981). Hydrogen and oxygen from water – V. The ROC system. *Energy* 6, 109–121. doi:10.1016/0360-5442(81)90131-6.

Phair, J. W., and Badwal, S. P. S. (2006). Review of proton conductors for hydrogen separation. *Ionics* 12 (2), 103–115. doi:10.1007/s11581-006-0016-4.

Rochelle, G., Chen, E., Freeman, S., Van Wagener, D., Xu, Q., and Voice, A. (2011). Aqueous piperazine as the new standard for CO_2 capture technology. *Chem. Eng. J.* 171 (3), 725–733. doi:10.1016/j.cej.2011.02.011.

Romero, M., and Steinfeld, A. (2012). Concentrating solar thermal power and thermochemical fuels. *Energy Environ. Sci.* 5 (11), 9234–9245. doi:10.1039/c2ee21275g.

Schulz, H. (1999). Short history and present trends of Fischer–Tropsch synthesis. *Appl. Catal. A Gen.* 186 (1), 3–12. doi:10.1016/s0926-860x(99)00160-x.

Steinfeld, A., and Palumbo, R. (2001). "Solar thermochemical process technology," in *Encyclopedia of physical science and technology* (Cambridge, MA: Academic Press), 237–256.

Sunarso, J., Baumann, S., Serra, J. M., Meulenberg, W. A., Liu, S., Lin, Y. S., et al. (2008). Mixed ionic–electronic conducting (MIEC) ceramic-based membranes for oxygen separation. *J. Membr. Sci.* 320, 13–41. doi:10.1016/j.memsci.2008.03.074.

Tan, X., and Li, K. (2007). Oxygen production using dense ceramic hollow fiber membrane modules with different operating modes. *AIChE J.* 53 (4), 838–845. doi:10.1002/aic.11116.

Tao, Z., Yan, L., Qiao, J., Wang, B., Zhang, L., and Zhang, J. (2015). A review of advanced proton-conducting materials for hydrogen separation. *Prog. Mater. Sci.* 74, 1–50. doi:10.1016/j.pmatsci.2015.04.002.

Tou, M., Jin, J., Hao, Y., Steinfeld, A., and Michalsky, R. (2019). Solar-driven co-thermolysis of CO_2 and H_2O and in-situ oxygen removal across a non-stoichiometric ceria membrane. *React. Chem. Eng.* 4, 1431–1438. doi:10.1039/C8RE00218E.

Tou, M., Michalsky, R., and Steinfeld, A. (2017). Solar-driven thermochemical splitting of CO_2 and in situ separation of CO and O_2 across a ceria redox membrane reactor. *Joule* 1 (1), 146–154. doi:10.1016/j.joule.2017.07.015.

Tuller, H. L. (2015). Solar to fuels conversion technologies. An MIT Future of Solar Energy Study Working Paper, Massachusetts Institute of Technology.

Venstrom, L. J., De Smith, R. M., Hao, Y., Haile, S. M., and Davidson, J. H. (2014). Efficient splitting of CO_2 in an isothermal redox cycle based on ceria. *Energy Fuels* 28 (4), 2732–2742. doi:10.1021/ef402492e.

Wang, H., Hao, Y., and Kong, H. (2015). Thermodynamic study on solar thermochemical fuel production with oxygen permeation membrane reactors. *Int. J. Energy Res.* 39 (13), 1790–1799. doi:10.1002/er.3335.

Zhu, L., Lu, Y., and Shen, S. (2016). Solar fuel production at high temperatures using ceria as a dense membrane. *Energy* 104, 53–63. doi:10.1016/j.energy.2016.03.108.

Conflict of Interest: The authors declare that the research was conducted in the absence of any commercial or financial relationships that could be construed as a potential conflict of interest.